Chinese Journal of Chemical Engineering 89 (2026) 112–122

Contents lists available at ScienceDirect

Chinese Journal of Chemical Engineering

journal homepage: www.elsevier.com/locate/CJChE

Full Length Article

Solid–liquid equilibrium and yield correlation model of melt crystallization of dimethylphenol isomer mixtures

Yuxi Zhang [1], Li Yang [2,*], Yixin Ma [2,3], Yan Zhang [2], Junya Cao [1], Jingcai Cheng [2,*], Chao Yang [2,3]

[1] School of Chemical and Environmental Engineering, China University of Mining and Technology, Beijing 100083, China
[2] State Key Laboratory of Petroleum Molecular & Process Engineering, Institute of Process Engineering, Chinese Academy of Sciences, Beijing 100190, China
[3] School of Chemical Engineering, University of Chinese Academy of Sciences, Beijing 100049, China

ARTICLE INFO

Article history:
Received 23 May 2025
Received in revised form
20 August 2025
Accepted 21 August 2025
Available online 12 September 2025

Keywords:
Melt crystallization
Yield
Dimethylphenols
Solid–liquid equilibrium
Thermodynamics models

ABSTRACT

Dimethylphenols serve as important intermediates in synthesizing pharmaceuticals and agrochemicals, yet traditional distillation struggles to separate their isomers due to minimal boiling point differences, and the development of melt crystallization is hampered by lacking solid–liquid equilibrium (SLE) data for some isomers. Therefore, the SLE data of both binary and ternary mixtures of 2,3-dimethylphenol (2,3-DMP), 3,5-dimethylphenol (3,5-DMP), and 3,4-dimethylphenol (3,4-DMP) were determined by using differential scanning calorimetry in this work. Additionally, crystallographic analysis was conducted to investigate the thermodynamic characteristics of these mixtures. The experimental results indicated that all the systems investigated in this research exhibited eutectic behavior. The experimentally obtained SLE data were well correlated with the Wilson and non-random two-liquid models. The excess thermodynamic functions were calculated to analyze the types and intensities of the molecular interactions occurring in the mixtures. Furthermore, this study developed a model for the correlation between the theoretical crystallization yield and the actual cooling yield and final yield in melt crystallization. This study has furnished reliable data essential for developing and optimizing the melt crystallization process of mixtures of 2,3-DMP, 3,5-DMP, and 3,4-DMP.

1. Introduction

Dimethylphenols serve as critical intermediates in industrial and agricultural applications, primarily used in the synthesis of resins, agrochemicals (*e.g.*, herbicides), pharmaceuticals (*e.g.*, vitamin E derivatives), and functional additives (*e.g.*, rubber antioxidants) [1,2]. With continuous advancements in applied research, their application domains are expanding across industries. The global demand for dimethylphenols has been increasing annually, with the market projected to grow at a compound annual growth rate (CAGR) of over 5% from 2023 to 2029 [3,4]. Their expanding utilization in chemical, pharmaceutical, and oilfield operations underscores their rising strategic significance in the global industrial landscape.

Dimethylphenols are typically produced in industry from coal tar and mixed phenols [5,6]. The conventional distillation technique struggles to separate dimethylphenol isomers effectively. Given the narrow boiling point differences of the studied isomers like 2,3-dimethylphenol (2,3-DMP), 3,5-dimethylphenol (3,5-DMP), and 3,4-dimethylphenol (3,4-DMP), this method incurs substantial energy consumption while failing to achieve sufficient purity. Consequently, a significant number of dimethylphenol distillation units have been phased out globally [7], driven by tightening environmental regulations and the limitations of conventional separation technologies. This underscores the critical demand for innovative, sustainable separation methods to address current challenges in DMP production. While melt crystallization also involves certain costs, such as cooling system maintenance and crystal layer control, a comprehensive economic analysis shows that it offers significant advantages over distillation. The energy consumption is typically 30% to 50% lower due to the elimination of vaporization requirements (latent heat

* Corresponding authors.
E-mail addresses: yangli@ipe.ac.cn (L. Yang), jccheng@ipe.ac.cn (J. Cheng).

https://doi.org/10.1016/j.cjche.2025.08.012

of vaporization ~50 kJ·mol^{-1} *vs*. latent heat of fusion ~20 kJ·mol^{-1} for dimethylphenols [7,8]). Equipment investment costs are also reduced due to simpler design and lower operating pressure requirements. Additionally, the achievable product purity (>99.5%) is higher than conventional distillation (>95%) [9]. Crystallization methods have become commonly utilized in modern times because of their energy-efficient processes and ability to yield substances with exceptional purity levels [10–15]. Melt crystallization is a solvent-free separation technique that achieves the separation goal by cooling and crystallizing from the molten state. It is especially suitable for systems in which the boiling points of individual components are close, and it can serve as an alternative to distillation for separation. In addition, melt crystallization has the potential for ultra-purification [11,16–18].

Solid–liquid equilibrium (SLE) data are the core elements for the separation of isomers through crystallization [19–24]. The operation conditions can be planned by analyzing the existence zones of substances in different states in the phase diagram [25]. Furthermore, SLE data can be used to quantify the changes of supersaturation during the melt crystallization process, thereby providing basic data for the kinetic studies of nucleation and crystal layer growth. Early studies focused on the fundamental property determination of dimethylphenol in pure substance form [8,26,27]. For mixture systems, Codoner *et al.* [28] revealed the polarization characteristics of dimethylphenols in dilute solutions through solvent dielectric constant and refractive index measurements, but this method is restricted to liquid-phase environments. Recent investigations have demonstrated enhanced comprehension of binary systems through experimental and theoretical analyses. Ma *et al.* [29] used differential scanning calorimetry (DSC) to obtain SLE data for 2,3-DMP, 2,5-DMP, and 2,6-DMP. Their findings confirmed these mixtures as simple eutectic systems. Shi *et al.* [7] further confirmed the absence of chemical interactions in the solid phase through infrared spectroscopy analysis. While previous studies have established fundamental frameworks for phenolic mixtures, three undercharacterized aspects emerge in practical applications. First, the thermodynamic database for dimethylphenol isomer systems, particularly the industrially prevalent 2,3-DMP, 3,5-DMP and 3,4-DMP mixtures, remains incomplete. This gap is pronounced given that 2,3-DMP and 3,4-DMP constitute more than 50% of crystalline impurities in isophorone-based 3,5-DMP synthesis. Second, the extrapolation of binary excess property models to multicomponent systems requires empirical validation. Third, prior research has not established a correlation between key process conditions in melt crystallization and thermodynamic characteristics, resulting in ambiguous guidance on process parameters.

For binary and ternary mixtures of 2,3-DMP, 3,5-DMP, and 3,4-DMP, the research utilizes DSC to investigate the SLE data, phase equilibrium characteristics and intermolecular interactions. These SLE data provide a key and effective tool for evaluating the feasibility of separating such mixtures through crystallization methods. Furthermore, the Wilson equation and the non-random two-liquid (NRTL) equation are adopted for data correlation and fitting to analyze the SLE data of the dimethylphenol systems in detail. These equations are also used for the calculation of excess thermodynamic functions, which help to reveal the types of interactions among different components within the mixtures and lay a solid foundation for the crystallization technology-based dimethylphenol separation process. Additionally, this study establishes a correlation between the theoretical crystallization yield and the actual cooling yield and final yield in melt crystallization, enabling the prediction of melt crystallization yields at different crystallization endpoint temperatures.

2. Materials and Methods

2.1. Materials

Table 1 lists the purity grades and sources of the chemicals. All materials were analytical grade and were employed directly for SLE determination without further purification, as confirmed by gas chromatography (GC, 7890B, Agilent, USA) analysis which detected no extraneous peaks.

2.2. DSC measurement

The binary and ternary mixtures were prepared *via* the gravimetric method. Samples were weighed using a Mettler-Toledo ME104/02 analytical balance (Switzerland, accuracy ±0.1 mg). The dimethylphenol mixture weighing 1 g was slowly heated in a glass tube with continuous stirring. Samples were maintained under nitrogen during preparation to prevent oxidation, then refrigerated for use.

The SLE data of both the binary and ternary mixtures were obtained using DSC (DSC 204F1, Metzsch, Germany). The instrument was calibrated using a multi-point calibration procedure with indium (melting point: 429.75 K, enthalpy of fusion: 28.45 J·g^{-1}), biphenyl (melting point: 342.41 K, enthalpy of fusion: 120.2 J·g^{-1}), bismuth (melting point: 544.55 K, enthalpy of fusion: 53.3 J·g^{-1}), and tin (melting point: 505.08 K, enthalpy of fusion: 60.46 J·g^{-1}) standards to ensure accuracy across the entire measurement temperature range. For DSC analysis, 4–6 mg solid samples were used. High-purity nitrogen at 50.0 ml·min^{-1} purged the system throughout the procedure. Samples were first heated at 10 K·min^{-1} to 10 K above the melting point of the mixture's higher-melting component, held for 10 min to eliminate DSC thermal history, then cooled at 1 K·min^{-1} to 40 K below the mixture's low melting point and held for another 10 min. After pretreatment, each sample was measured at a 1 K·min^{-1} heating rate [7]. A slow scanning rate was selected to approximate equilibrium measurement conditions, minimize kinetic effects [30], and enhance the accuracy of melting enthalpy evaluation.

2.3. Raman spectroscopy analysis

Raman spectra (EPD-785P, Uropod, China) of pure 3,5-DMP, 2,3-DMP, 3,4-DMP, and their binary mixtures were measured in this study. These raw spectra underwent a preprocessing workflow consisting of baseline correction and normalization. The baseline correction was implemented *via* a segmented iterative polynomial fitting method, where first-order polynomial baselines were constructed for each spectral segment. This staged processing approach optimized baseline drift compensation and ensured data consistency across different measurement batches. Subsequent area normalization was performed by calculating the integrated intensity within the 300–2500 cm^{-1} spectral range and normalizing the entire spectrum to this value.

2.4. The melt crystallization procedure

The melt crystallization experiments were performed in a tube crystallizer (length: 100 mm, inner diameter: 40 mm, glass thickness: 1.3 mm). The temperature of the crystallizer was controlled by a circulator bath (CBC 5, IKA, Germany) connected to the jacket of the crystallizer with an accuracy of ±0.02 K. The initial mixture contained 96% (mass) 3,5-DMP as the main component, with 2% (mass) 2,3-DMP and 2% (mass) 3,4-DMP as the main impurities. The concentrations were determined by GC (FID, DB-FFAP, Agilent). The crystallization process began by cooling the mixture

Table 1
Details of chemicals employed in this work.

Chemical name	CAS number	Molecular formula	Molecular weight/g·mol^{-1}	Source	Mass fraction purity
2,3-DMP	526-75-0	$C_8H_{10}O$	122.16	Shanghai Macklin Biochemical co., Ltd., China	≥0.99
3,5-DMP	108-68-9				
3,4-DMP	95-65-8				

to the endpoint temperature tend at a rate of 2 K·h^{-1}. The temperature was maintained for 1 h to ensure complete crystallization, after which the mother liquor was discharged, with the mass of the discharged mother liquor being m_d. For the sweating treatment, the temperature was increased to 335.15 K at a rate of 5 K·h^{-1} and held for 1 h before discharging the sweat.

3. Theoretical Basis

Below the phase transition temperature, the SLE curves of the studied binary mixtures are calculated using Eq. (1) [31]:

$$\ln \gamma_i x_i = \frac{\Delta H_{m,i}}{RT}\left(\frac{T}{T_{m,i}} - 1\right) - \frac{\Delta C_{p,i}}{R}\left(\ln\frac{T_{m,i}}{T} - \frac{T_{m,i}}{T} + 1\right) \tag{1}$$

where x_i and γ_i are respectively the mole fraction and the activity coefficient of component i at temperature T, $\Delta H_{m,i}$ is the molar melting enthalpy, $\Delta C_{p,i}$ represents the heat capacity difference between the liquid and solid phases of component i at its melting point, R is the universal gas constant, and $T_{m,i}$ is the melting absolute temperature. Eq. (1) applies to simple eutectic mixtures that are completely immiscible in the solid phase. The term involving $\Delta C_{p,i}$ is substantially smaller in value when compared with the other terms [32]. During subsequent analysis, disregarding this minor discrepancy and focusing solely on the first term in Eq. (1) allows simplification of the analysis while maintaining results accuracy, leading to Eq. (2).

$$\ln \gamma_i x_i = \frac{\Delta H_{m,i}}{RT}\left(\frac{T}{T_{m,i}} - 1\right) \tag{2}$$

The Wilson model and the NRTL model were utilized to correlate the liquid-phase activity coefficients of the binary systems under research in this work. Assuming the mixtures exhibit ideal mixing behavior, all the activity coefficients are equal to 1 ($\gamma_i \approx 1$). Besides activity coefficients, key excess thermodynamic functions—such as excess Gibbs energy (G^E), enthalpy (H^E), and entropy (S^E)—are used to characterize differences in thermodynamic properties between real and ideal systems under the same temperature and pressure. These functions assess deviations from ideal behavior and help identify dominant intermolecular interactions [33]. This study characterized the behavior of these functions in ternary/binary mixtures, exploring how intermolecular interactions influence energy evolution and structural ordering during mixing processes.

The activity coefficients calculated using the Wilson model equation [34] are given by Eqs. (3) and (4):

$$\ln \gamma_i = 1 - \ln\left(\sum_{j=1}^{N_C} \Lambda_{ij} x_j\right) - \sum_{k=1}^{N_C} \frac{\Lambda_{ki} x_k}{\sum_{j=1}^{N_C} \Lambda_{kj} x_j} \tag{3}$$

$$\Lambda_{ij} = \frac{V_j^L}{V_i^L}\exp\left[\frac{-\left(\lambda_{ij} - \lambda_{ii}\right)}{RT}\right] \tag{4}$$

where, V_i^L and V_j^L respectively denote the molar volumes (m^3·mol^{-1}) of component i and j. Since the two components used in this paper are isomers, $V_j^L/V_i^L = 1$. γ_i is the activity coefficient of component i, x_i is the mole fraction of component i. The adjustable parameters of the Wilson model are $\Delta\lambda_{ij} = \lambda_{ij} - \lambda_{ii}$. N_C is the number of components.

The NRTL equation relies on the local composition model [35]. The values of the activity coefficients γ_i are given by the following Eqs. (5)–(7):

$$\ln \gamma_i = \frac{\sum_j^{N_C} \tau_{ji} G_{ji} x_j}{\sum_k^{N_C} G_{ki} x_k} + \sum_j^{N_C} \frac{G_{ij} x_j}{\sum_k^{N_C} G_{kj} x_k}\left(\tau_{ij} - \frac{\sum_l^{N_C} \tau_{lj} G_{lj} x_l}{\sum_k^{N_C} G_{kj} x_k}\right) \tag{5}$$

$$G_{ij} = \exp\left(-\alpha_{ij}\tau_{ij}\right) \tag{6}$$

$$\tau_{ij} = \frac{g_{ij} - g_{jj}}{RT} = \frac{\Delta g_{ij}}{RT} \tag{7}$$

where x_j is the mole fraction, G_{ij} and τ_{ij} are the model parameters, g_{ij}, g_{jj} is the energy parameter, Δg_{ij} represents the interaction energy. The parameter α_{ij}, which relates to the non-random nature of the mixture, has a value range of 0.2–0.47 [30,36], and $\alpha_{ij} = \alpha_{ji}$.

The Wilson equation utilizes interaction parameters $\Delta\lambda_{ij}$ and $\Delta\lambda_{ji}$, while the NRTL equation has parameters α_{ij}, Δg_{ij} and Δg_{ji}. The values are calculated by minimizing the objective functions through the Nelder–Mead simplex method [37]:

$$F_{obj} = \sum_{i=1}^{N}\left(T_i^{cal} - T_i^{exp}\right)^2 \tag{8}$$

The temperature root mean square deviation (RMSD) is [38]:

$$\sigma_T = \left[\frac{1}{N}\sum_{i=1}^{N}\left(T_i^{exp} - T_i^{cal}\right)^2\right]^{\frac{1}{2}} \tag{9}$$

where N represents the count of experimental data points.

4. Results and Discussion

4.1. Thermal properties of pure compounds

For pure compounds 2,3-DMP, 3,5-DMP and 3,4-DMP, their melting temperatures and enthalpies were determined *via* DSC. Table 2 contrasts the experimental values with those from the literature to evaluate the accuracy of the experimental data. Using Eq. (10), the average relative deviation (ARD) between experimental and literature values was calculated. ARD values for melting temperature and solid–liquid phase transition enthalpy were 0.15% and 0.34%, respectively. This demonstrates that the measurement methods and operation procedures adopted in this experiment possess high reliability, and the obtained data can

Table 2
Thermophysical properties of the materials measured *via* DSC: melting temperature (T_m) and enthalpy of fusion ($\Delta_{fus}H$) at p = 100.05 kPa.

Composition	$\Delta_{fus}H$/kJ·mol^{-1}		T_m/K	
	Experimental data	Literature data	Experimental data	Literature data
2,3-DMP	21.015	21.024 [26] 21.020 [39]	345.65	346.00 [26] 345.95 [39] 345.45 [28] 345.68 [8]
3,5-DMP	17.789	17.997 [26] 18.000 [39] 17.422 [27] 17.877 [7]	336.37	336.80 [26] 336.75 [39] 336.15 [28] 336.39 [8] 336.59 [27] 336.47 [7]
3,4-DMP	17.986	18.127 [26] 18.130 [39]	337.97	334.00 [26] 333.95 [39] 338.15 [28] 338.24 [8]

The standard uncertainties, $u(T)$ = 0.50 K, $u(\Delta H)$ = 2.5 J·g^{-1}, $u(p)$ = 0.05 MPa.

provide support for subsequent relevant research and applications.

$$\mathrm{ARD} = \frac{1}{m}\sum_{i=1}^{m}\left|\frac{T_{i,\mathrm{exp}} - \overline{T}_{i,\mathrm{lit}}}{T_{i,\mathrm{exp}}}\right| \times 100\% \quad (10)$$

4.2. Binary mixtures

4.2.1. Crystallographic analysis

Raman spectroscopy analysis was specifically carried out to explore whether reactions occur among the components of pure components and eutectic mixtures under the corresponding states. Fig. 1 shows the Raman spectral profiles of the three individual pure components alongside their corresponding binary eutectic mixtures.

In the low wavenumber region (500–1000 cm^{-1}), corresponding to the molecular skeletal vibrational characteristics, significant differences in peak positions and intensities were observed among 3,5-DMP, 2,3-DMP, and 3,4-DMP. For instance, 3,5-DMP exhibited a strong characteristic peak near 1000 cm^{-1}, 3,4-DMP showed a prominent peak at approximately 945 cm^{-1}, and 2,3-DMP displayed a distinct peak at 1091 cm^{-1}. This difference arises from the influence of methyl substitution positions on molecular skeletal symmetry and vibration modes. In the Raman spectra of the binary eutectic mixtures formed from the three pure components, the characteristic peaks of 2,3-DMP, 3,5-DMP, and 3,4-DMP were fully retained, with only component peak superposition observed. Theoretically, Raman spectroscopy reflects molecular vibrations and rotations. Chemical interactions would alter vibration modes, leading to new peaks distinct from the original components. The absence of such peaks in the mixtures supports the conclusion that the components remained in a physical mixing state without chemical interactions after melting.

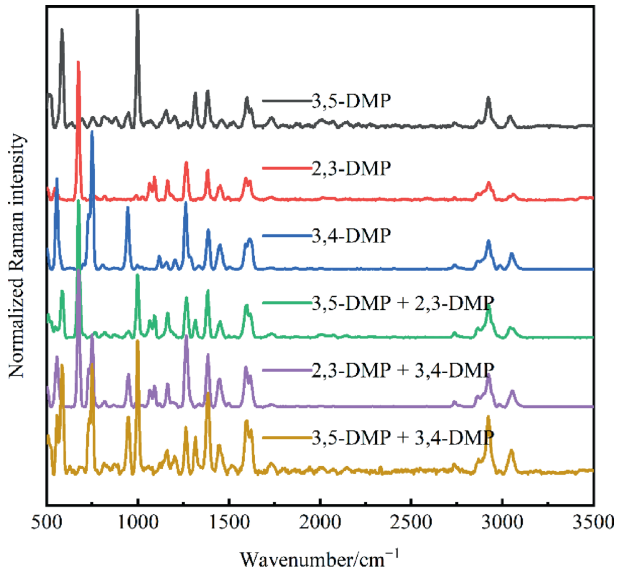

Fig. 1. Raman spectra of pure 3,5-DMP, 2,3-DMP, 3,4-DMP and the three binary mixtures.

4.2.2. Binary solid–liquid phase diagram and thermodynamic modeling

Figs. S1–S3 (in Supplementary Material) present the Tammann plots of the three binary systems, which enable identification of eutectic points in their phase diagrams. The eutectic compositions (x_{eu}, mole fraction of the first-listed component) of the binary systems 3,5-DMP + 2,3-DMP, 3,5-DMP + 3,4-DMP, and 2,3-DMP + 3,4-DMP are 0.6029, 0.4972, and 0.4173, respectively.

Tables S1–S3 present the experimental SLE data and the derived activity coefficients for three binary systems. Fig. S4 compares the activity coefficients of different components in three binary dimethylphenol systems. The results show that activity coefficients generally exhibit negative deviations from thermodynamic ideality (*i.e.*, $\gamma < 1$), while approaching unity near the pure-component limits. The experimental data were correlated using the Wilson model and the NRTL model. Figs. S5–S7 show the DSC curves obtained from the three binary mixtures. For the binary mixture samples, their DSC curves all show two distinct endothermic peaks. While the liquidus temperature changes with composition, the eutectic temperature remains relatively stable, as indicated by the second and first peaks in the DSC curve, respectively.

Figs. 2–4 display the phase diagrams of the three binary mixtures derived from experiments and fitting using the Wilson and NRTL models. In the figures, there is only one inflection point in each of these three binary systems. All the studied systems show negative deviations from the ideal state, in which the activity coefficient is assumed to be 1 for thermodynamic calculations. Curve fitting results in the figures show that Wilson and NRTL equations effectively model the liquidus of binary systems.

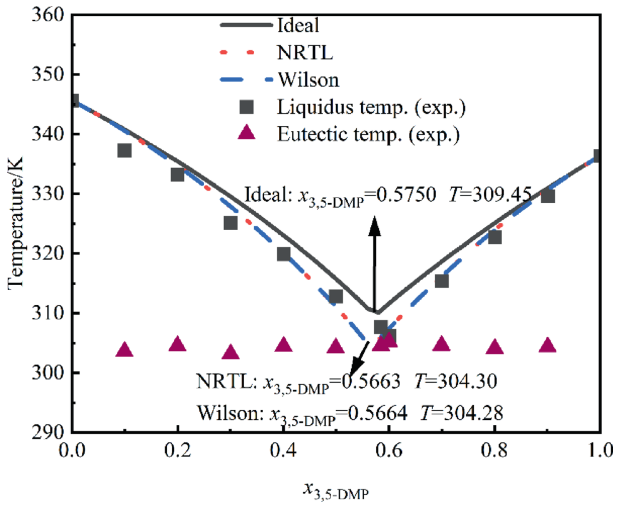

Fig. 2. Experimental and model-derived SLE phase diagrams for 3,5-DMP + 2,3-DMP.

Table 3 lists the parameters and the RMSD values of all the models. In the 3,5-DMP + 2,3-DMP mixture, Wilson's liquidus fitting RMSD (1.60 K) is notably lower than the ideal model's 3.01 K and marginally lower than NRTL's 1.61 K, demonstrating its moderate advantage over NRTL and clear superiority over the ideal model within this binary system. The remaining two binary mixtures show similar results. The Wilson model, incorporating two adjustable parameters, can be flexibly adapted to the characteristics of different systems to a certain extent to achieve a good fitting effect. Although the NRTL equation theoretically has more room for adjustment, within the specific parameter range (α_{12} is between 0.2 and 0.47) involved in this study, the fitting effect of the Wilson model and the NRTL model shows little difference in reflecting the actual variation law of the liquidus of the binary systems.

4.3. Ternary mixtures

4.3.1. Ternary solid–liquid phase diagram and thermodynamic modeling

Fig. S8 presents the DSC curves and Table S4 provides the SLE data for the ternary system consisting of 3,5-DMP, 2,3-DMP and 3,4-DMP. The curves exhibit two endothermic peaks: the onset temperature of the first peak corresponds to the eutectic temperature (280.6 K), while the second peak corresponds to the melting temperature of the ternary mixture, indicating that the mixture displays simple eutectic behavior. Fig. 5 presents the 3D diagram of the ternary system. The eutectic temperatures of the binary systems are as follows: 304.28 K for the 3,5-DMP + 2,3-DMP mixture, 306.35 K for the 2,3-DMP + 3,4-DMP mixture, and 294.66 K for the 3,5-DMP + 3,4-DMP mixture. The ternary system comprising these three components exhibits a depressed eutectic temperature of 280.6 K. Given the principle of melting-point depression, within a ternary system, multiple components engage in intricate interactions. During the crystallization phase, these interactions lead to a highly convoluted molecular arrangement. Consequently, the long-range order inherent in the crystalline lattice becomes substantially disrupted. This disruption of crystallographic order effectively lowers the energy barrier required for the solid-to-liquid phase transition, thereby causing melting to occur at a relatively lower temperature. The SLE phase diagram of the ternary system of 3,5-DMP, 2,3-DMP and 3,4-DMP exhibits the characteristic that the liquidus is the lowest at the middle position among the three components. Specifically, the lowest temperature point is observed in the composition consisting of 33.41% 3,5-DMP, 27.45% 2,3-DMP and 39.14% 3,4-DMP. These phase equilibrium data enable theoretical yield prediction for different feed compositions and crystallization temperatures, facilitate the determination of minimum cooling temperature requirements, and support the design of multi-stage crystallization processes.

The SLE data of the ternary mixture were subjected to correlation analysis using the Wilson model and the NRTL model. Ternary system model parameters matched those of the binary system. Fig. 6 illustrates the ternary mixture modeling results, where both Wilson and NRTL models effectively characterize the system, demonstrating favorable accuracy in liquidus temperature fitting. The Wilson model exhibited a prediction deviation of 0.59%, and the NRTL model showed 0.60% deviation. The RMSD values are 2.36 K and 2.44 K, respectively, while the RMSD of the ideal model is 4.44 K. By comprehensively comparing the relevant deviation data of each model, it can be determined that the Wilson model exhibits better performance in fitting the ternary system.

4.3.2. Excess thermodynamic function

By evaluating the excess thermodynamic properties, including G^E, H^E, and S^E, the measurement and properties of molecular

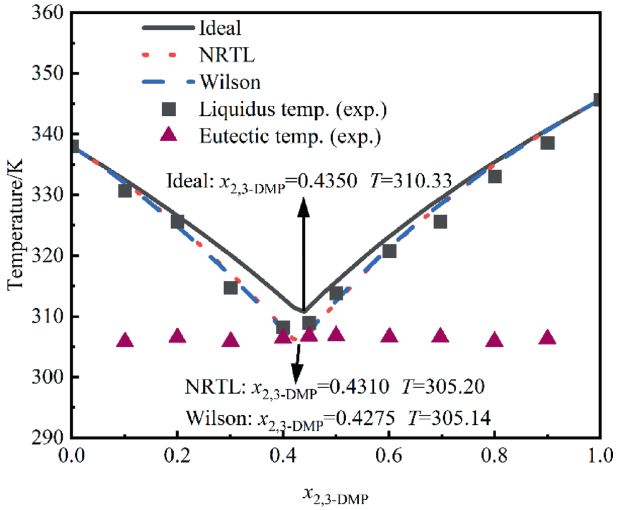

Fig. 3. Experimental and model-derived SLE phase diagrams for 2,3-DMP + 3,4-DMP.

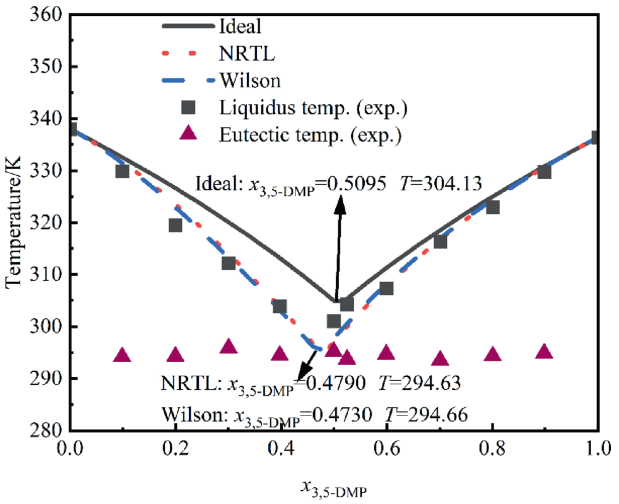

Fig. 4. Experimental and model-derived SLE phase diagrams for 3,5-DMP + 3,4-DMP.

interactions in binary or ternary mixtures can be effectively highlighted, and their deviations from the ideal behavior can be well reflected. While activity coefficients describe localized non-ideality of individual components, they lack the capacity to correlate with macroscopic thermodynamic behavior. In contrast, excess thermodynamic properties quantify the differences between the actual and ideal behavior of the system, reflecting the comprehensive effects of intermolecular interactions from multiple perspectives, such as energy (Gibbs energy), heat effects (enthalpy), and disorder (entropy).

The excess mixing properties can be evaluated using Eqs. (11)–(13).

$$G^{E} = RT\sum(x_i \ln \gamma_i) \tag{11}$$

$$H^{E} = -RT^2\left[\frac{\partial\left(G^{E}/RT\right)}{\partial T}\right]_{x_1,p} \tag{12}$$

$$TS^{E} = H^{E} - G^{E} \tag{13}$$

Figs. S9–S11 show the excess thermodynamic properties of the system calculated by using the Wilson and NRTL models under different mole fractions. It can be known that these two models exhibit a high degree of similarity in both qualitative and quantitative analyses. The trends of the excess thermodynamic properties changing with the mole fraction reflected by the two models are consistent, and both can reflect the deviation characteristics of the system from the ideal behavior under different composition conditions. Through data comparison and analysis, it can be found that the absolute value of the excess enthalpy calculated by the Wilson model is slightly larger. This discrepancy highlights the nuanced differences between the two models when describing intermolecular interactions and the thermodynamic properties of the systems.

The ternary 3,5-DMP + 2,3-DMP + 3,4-DMP system demonstrates analogous trends with negative excess properties, as presented in Figs. 7–9. Both NRTL and Wilson models demonstrate good consistency in predicting G^{E}; however, the Wilson model yields systematically lower H^{E} values compared with the NRTL model.

The excess thermodynamic functions (G^{E}, H^{E}, S^{E}) provide critical insights into the nonideal mixing behavior of the systems. All systems exhibit negative G^{E} values, indicating spontaneous mixing processes, while the consistently negative H^{E} values (reaching up to −1000 J·mol^{-1}) suggest exothermic interactions, likely arising from hydrogen bonding or other specific intermolecular forces [33,40]. The observed $S^{E} < 0$ further implies the formation of short-range ordered structures during mixing, leading to reduced configurational entropy. Thermodynamic analysis reveals a contrast between the peak values of $|H^{E}|$ (1000 J·mol^{-1}) and $|TS^{E}|$ (400–500 J·mol^{-1}) near the eutectic composition. The absolute values of H^{E} significantly exceed those of TS^{E} across all compositions, demonstrating enthalpy-driven dominance in these systems. Notably, 3,4-DMP displays markedly stronger deviations from ideality compared to other components — its mixtures with 3,5-DMP and 2,3-DMP generate substantially larger $|H^{E}|$ (650–1000 J·mol^{-1}) and $|TS^{E}|$ (400–500 J·mol^{-1}), whereas the 3,5-DMP + 2,3-DMP system shows weaker effects ($H^{E} \approx -350$ J·mol^{-1}, $TS^{E} \approx -30$ J·mol^{-1}). No eutectic minima occur in ternary excess functions, though a S^{E} minimum near 0.3 (3,5-DMP), 0.02 (2,3-DMP), 0.68 (3,4-DMP) suggests preferential ordering between 3,5-DMP and 3,4-DMP. This pronounced contrast highlights the unique role of 3,4-DMP in enhancing nonideal interactions, potentially attributed to its distinct substitution pattern that facilitates stronger molecular associations. Such fundamental understanding of the thermodynamic driving forces is essential for designing functional multicomponent systems with tailored properties.

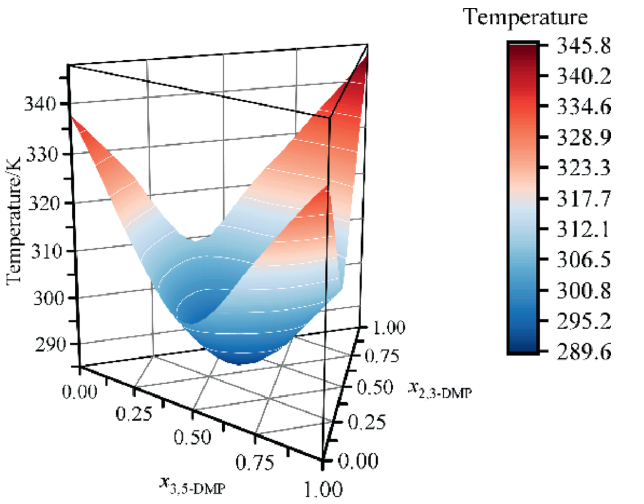

Fig. 5. 3D plots of the ternary mixture of 3,5-DMP, 2,3-DMP and 3,4-DMP.

4.4. Melt crystallization: yield modeling and endpoint temperature design

Based on the Wilson model's superior performance (0.59% deviation *vs.* 0.60% for NRTL) and its practical advantages as a two-parameter model (compared to NRTL's three parameters), the theoretical yields of 3,5-DMP under various crystallization conditions were calculated based on this model and compared with the actual melt crystallization yields.

Based on the thermodynamic theory of ternary phase diagrams, the theoretical maximum yield of 3,5-DMP at different crystallization endpoint temperatures is calculated through the following steps. In the ternary phase diagram coordinate system, the pure 3,5-DMP component point and the initial mixture composition

Table 3
Correlation of the SLE data for the three binary mixtures using ideal, Wilson and NRTL models: binary interaction parameters and RMSD.

System	Parameters					RMSD/K		
	Wilson		NRTL			Ideal	Wilson	NRTL
	$\Delta\lambda_{12}$/J·mol^{-1}	$\Delta\lambda_{21}$/J·mol^{-1}	Δg_{12}/J·mol^{-1}	Δg_{21}/J·mol^{-1}	α_{12}			
3,5-DMP +2,3-DMP	−1028.43	−212.54	−202.96	−1043.60	0.47	3.01	1.60	1.61
2,3-DMP +3,4-DMP	2373.51	−2501.80	−2276.01	1784.53	0.47	2.84	1.50	1.56
3,5-DMP +3,4-DMP	3230.12	−3368.31	−3171.85	2417.18	0.47	4.53	1.90	2.22

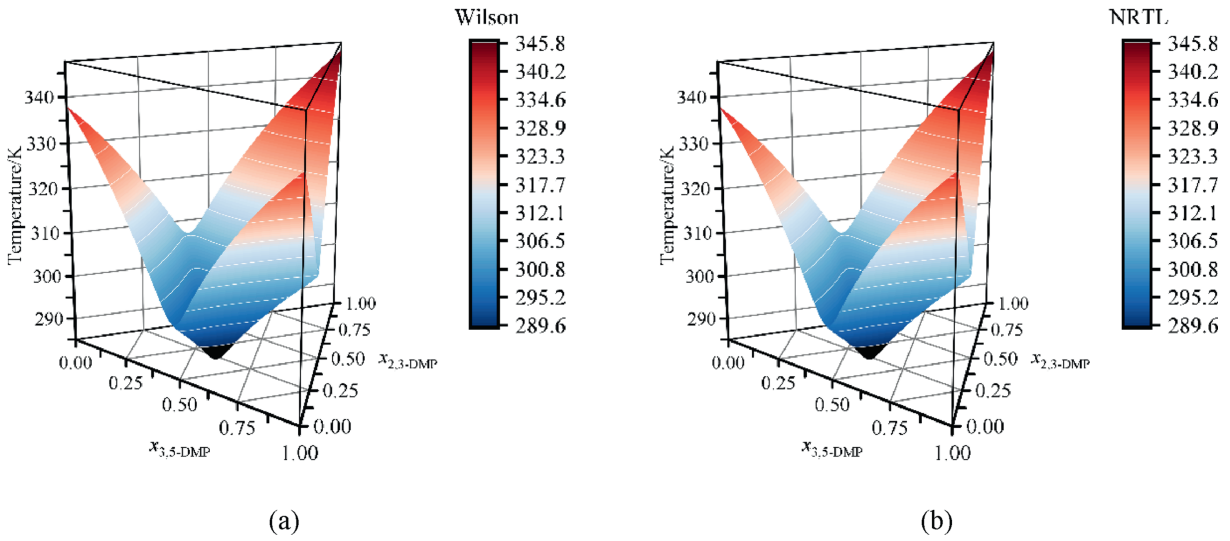

Fig. 6. Model predictions of 3,5-DMP, 2,3-DMP and 3,4-DMP ternary mixture: (a) Wilson model predictions; (b) NRTL model predictions.

point are connected with a straight line. The intersection of this line with the corresponding isotherm represents the phase equilibrium state of the system, as shown in Fig. 10. Under the assumption of an ideal crystallization process, where only pure 3,5-DMP crystals are precipitated, the lever rule was used to obtain the quantitative relationship between the mass of 3,5-DMP crystals and the total mass of the system. The yield was calculated according to the ratio of the mass of 3,5-DMP crystals and the mass of 3,5-DMP in the initial material:

$$w_t = \frac{m_t}{m \times c_{feed}} \tag{14}$$

where w_t is the theoretical yield of 3,5-DMP; m_t is the mass of 3,5-DMP crystals calculated using the lever rule of the phase diagram; m is the total mass of the initial material; and c_{feed} is the mass fraction of 3,5-DMP in the initial material.

The mass of the discharged mother liquor and the mass of the crystalline layer m_{cry} satisfy the mass conservation relationship: $m = m_{cry} + m_d$. The cooling crystallization yield, w_c is defined as the ratio of the mass of the crystal layer after reaching the crystallization endpoint temperature to the mass of the target product in the initial material:

$$w_c = \frac{m_{cry}}{m \times c_{feed}} \tag{15}$$

After sweating, a crystalline mass m_{final} with higher purity is obtained. Taking into account the purity of the crystals after sweating c_{final}, the final yield is calculated as follows:

$$w_f = \frac{m_{final} \times c_{final}}{m \times c_{feed}} \tag{16}$$

Through the calculation methods of theoretical and actual yield described above, a systematic analysis of data at different crystallization endpoint temperatures can be conducted to deeply explore the yield variation patterns of this melt crystallization process.

As shown in Fig. 11, the compositional data of the mother liquor corresponding to different crystallization endpoint temperatures are annotated in the phase diagram constructed by Wilson fitting. Experimental measurements reveal that the 3,5-DMP content in

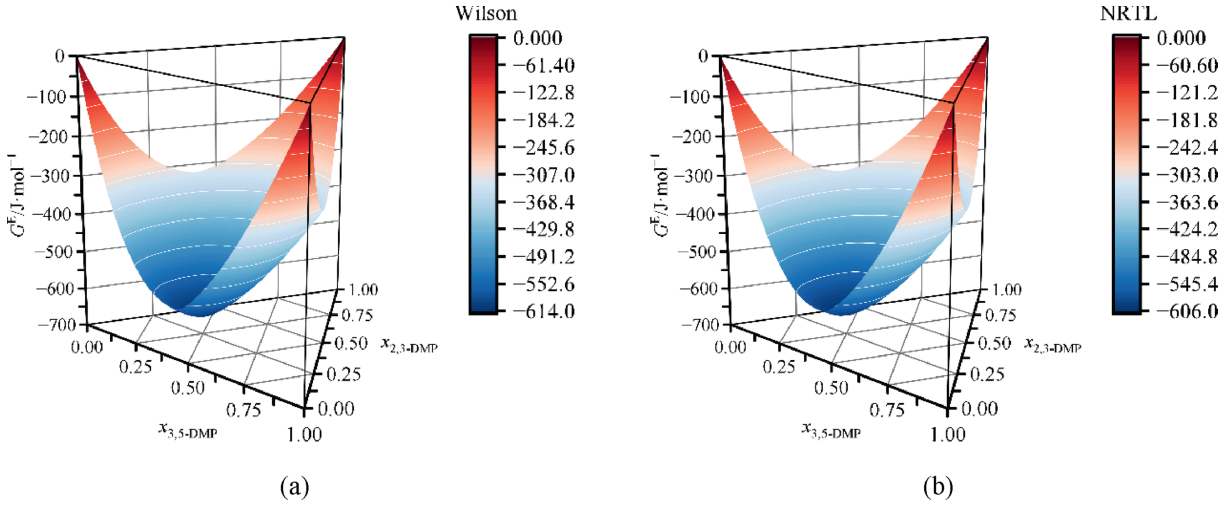

Fig. 7. Excess Gibbs free energy of the ternary mixture of 3,5-DMP, 2,3-DMP and 3,4-DMP: (a) Wilson model predictions; (b) NRTL model predictions.

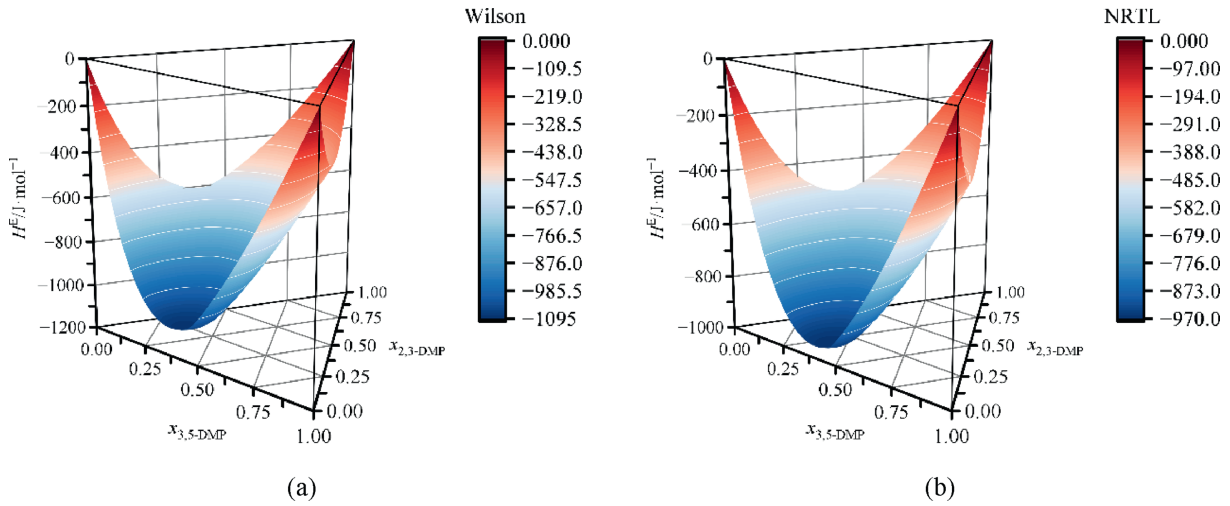

Fig. 8. Excess enthalpy of the ternary mixture of 3,5-DMP, 2,3-DMP and 3,4-DMP: (a) Wilson model predictions; (b) NRTL model predictions.

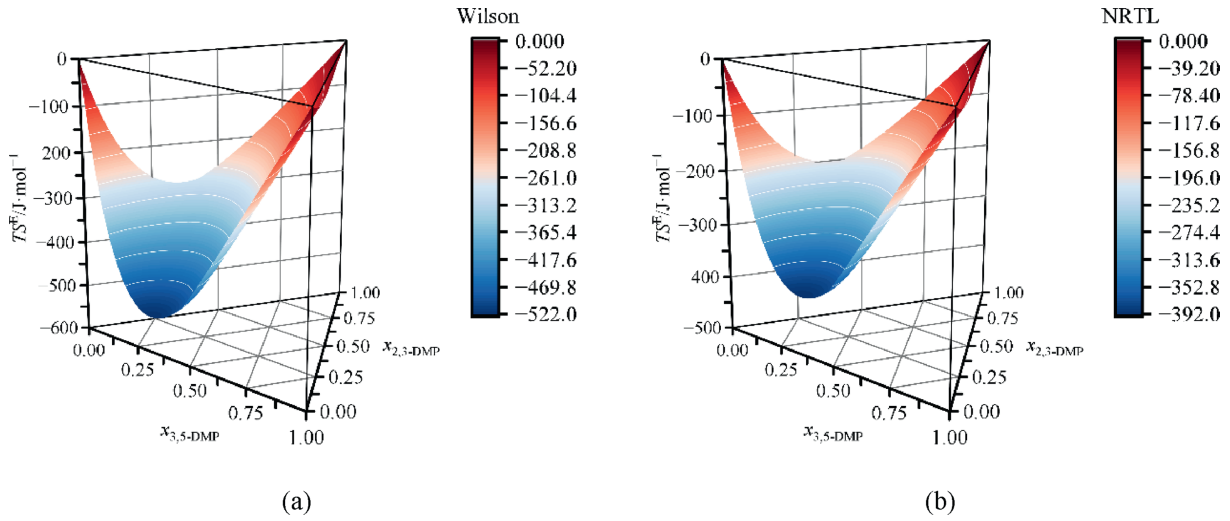

Fig. 9. Excess entropy of the ternary mixture of 3,5-DMP, 2,3-DMP and 3,4-DMP: (a) Wilson model predictions; (b) NRTL model predictions.

the mother liquor significantly exceeds the theoretical values derived from the phase diagram, specifically manifested by the fact that all experimental data points lie below the solid-liquid equilibrium surface of the phase diagram. This phenomenon indicates that the melt crystallization process has not reached thermodynamic equilibrium. When the crystallization endpoint temperature is above 321.45 K, the deviation between the mother liquor composition and the theoretical values of the phase diagram is relatively small, suggesting that the system can easily achieve an approximate equilibrium state. As the crystallization endpoint temperature gradually decreases, however, the degree of deviation between the experimental data points and the solid–liquid equilibrium surface of the Wilson phase diagram becomes increasingly significant.

The underlying cause of these discrepancies is fundamentally linked to the kinetic mechanisms governing the crystallization process. Lower crystallization endpoint temperatures lead to larger thickness of the crystal layer in melt crystallization, which not only significantly increases the thermal resistance during crystallization but also substantially prolongs the time required for the system to reach thermodynamic equilibrium. Although the deviation between the mother liquor composition and the theoretical values continues to increase with decreasing crystallization endpoint temperature, the experimental data points still retain the characteristic of distributing along the trend of the equilibrium phase diagram surface. This fully demonstrates that the deviations between the mother liquor composition and the equilibrium phase diagram are predominantly governed by the kinetic conditions in the actual crystallization process.

As shown in Fig. 12, the research results indicate a significant correlation between the crystallization endpoint temperature and the yield of 3,5-DMP. As T_{end} decreases, the theoretical yield, cooling crystallization yield, and final yield all show a monotonically increasing trend, indicating that a lower temperature environment is more conducive to the crystallization and separation of the target product. However, there is a lower limit for the temperature, which must not be lower than the eutectic temperature. It is worth noting that when T_{end} < 309.95 K, the cooling crystallization yield exceeds 100%, which is caused by the entrainment of mother liquor in the crystal layer. This phenomenon leads to a calculated mass of the target product higher than the initial charge. In contrast, the final yield always remains within

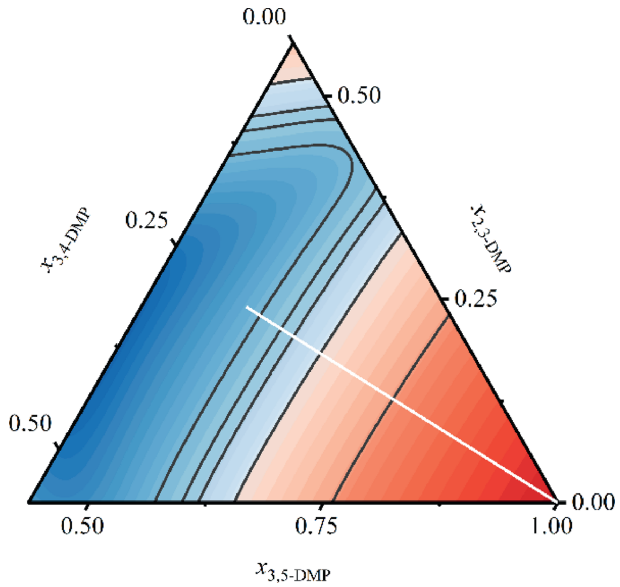

Fig. 10. Ternary phase diagram for calculating the theoretical yield of 3,5-DMP using the lever rule.

the threshold range of the theoretical yield, which fully verifies that the sweating operation can effectively remove the entrained and adhered mother liquor between the crystals. It should be noted that partial remelting of the crystallized 3,5-DMP during the sweating process is the direct reason why the final yield is always lower than the theoretical yield. In melt crystallization processes, even when operating under non-equilibrium conditions, a pronounced correlation persists between the final yield and the theoretical yield under identical crystallization and sweating protocols. This observation underscores the fundamental guiding role of thermodynamics in kinetic systems, demonstrating that

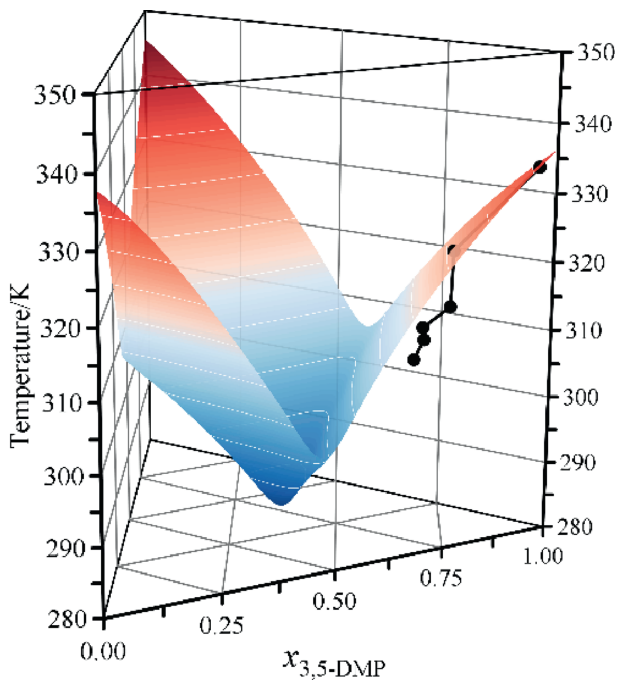

Fig. 11. Phase diagram from Wilson fitting with mother liquor compositions at different crystallization endpoint temperatures.

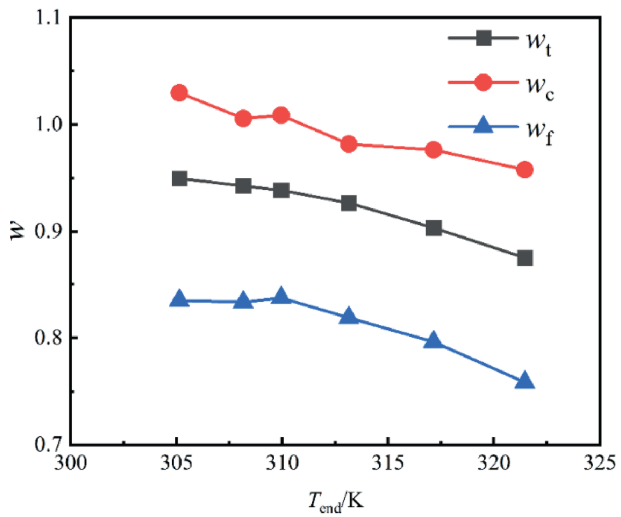

Fig. 12. Relationship between crystallization endpoint temperature and yields of 3,5-DMP.

thermodynamic principles retain their predictive power for process directionality and trend analysis even in non-equilibrium kinetic regimes.

Linear regression analysis was conducted for the cooling crystallization yield and final yield individually against the theoretical yield, as illustrated in Fig. 13. Before sweating, the relationship between the cooling crystallization yield and the theoretical yield shows an *R*-squared value of 0.87, indicating a moderate linear correlation. The observed scatter primarily stems from the inherent characteristics of the crystallization process, specifically slight fluctuations in growth rate under non-equilibrium conditions. Therefore, there exist some differences in the crystal layer thickness and porosity, affecting mother liquor entrainment. After the sweating treatment, the relationship between the final yield and the theoretical yield exhibits an *R*-squared value increasing to 0.97, demonstrating a significantly improved correlation. This enhancement is achieved through the sweating process, which eliminates kinetic effects and reduces mother liquor entrainment, bringing the system closer to equilibrium conditions predicted by the phase diagram. The high correlation of the final yield data

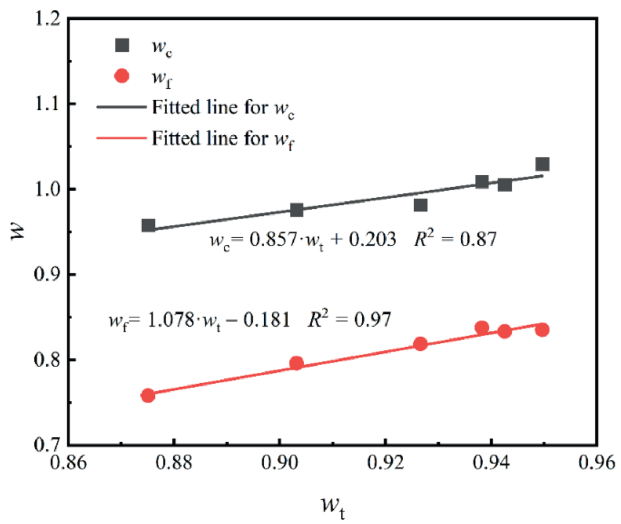

Fig. 13. Linear regression of yield relationships in 3,5-DMP crystallization.

validates the reliability of the Wilson model-based phase diagram calculations, suggesting that this theoretical approach can effectively predict the melt crystallization process outcomes.

5. Conclusions

This paper systematically investigated the SLE of binary and ternary mixtures of 3,5-DMP, 2,3-DMP and 3,4-DMP. Experimental measurements were performed using DSC, with subsequent thermodynamic modeling through the Wilson and NRTL activity coefficient models. The Wilson and NRTL models exhibited RMSD values of 1.50–1.90 K and 1.56–2.22 K, respectively, compared to 2.84–4.53 K for the ideal model. For the ternary system, the RMSD values for the Wilson and NRTL models are 2.36 K and 2.44 K, respectively, while the RMSD of the ideal model is 4.44 K. This demonstrates that the Wilson and NRTL models are capable of accurately depicting the relevant thermodynamic properties and phase behavior characteristics of this system.

In addition, the excess thermodynamic functions (G^E, H^E, S^E) were calculated to analyze the types and intensities of the molecular interactions occurring in the mixtures. The ternary mixtures exhibit negative excess properties, featuring spontaneous and exothermic mixing with negative enthalpy-driven dominance. 3,4-DMP significantly enhances nonideal interactions due to its unique substitution pattern, leading to notably larger $|H^E|$ and $|TS^E|$ values when mixed with other components.

Analysis of the phase diagrams for the three binary systems revealed the presence of simple eutectic behavior, indicating that melt crystallization represents a viable separation method for dimethylphenol mixtures. Then, the melt crystallization and sweating processes were carried out to purify 3,5-DMP. Notably, the final yield demonstrates a strong correlation with the theoretical yield, with an *R*-squared value of 0.97, enabling the determination of the key melt crystallization process parameter—crystallization endpoint temperature—based on the theoretical yield and target yield.

CRediT Authorship Contribution Statement

Yuxi Zhang: Writing – original draft, Methodology, Investigation, Formal analysis. Li Yang: Writing – review & editing, Supervision, Resources, Data curation. Yixin Ma: Software, Formal analysis. Yan Zhang: Writing – review & editing. Junya Cao: Writing – review & editing. Jingcai Cheng: Writing – review & editing, Supervision, Methodology, Funding acquisition, Data curation. Chao Yang: Writing – review & editing, Supervision, Resources, Funding acquisition.

Declaration of Competing Interest

The authors declare that they have no known competing financial interests or personal relationships that could have appeared to influence the work reported in this paper.

Acknowledgements

This research was funded by the National Natural Science Foundation of China (22308358, 22208346, 22421003), IPE Project for Frontier Basic Research (QYJC-2023-05) and CAS Project for Young Scientists in Basic Research (YSBR-038).

Supplementary Material

Supplementary data to this article can be found online at https://doi.org/10.1016/j.cjche.2025.08.012.

References

[1] O.A. Kholdeeva, N.N. Trukhan, M.P. Vanina, V.N. Romannikov, V.N. Parmon, J. Mrowiec-Białoń, A.B. Jarzębski, A new environmentally friendly method for the production of 2,3,5-trimethyl-*p*-benzoquinone, *Catal. Today* 75 (1–4) (2002) 203–209.
[2] B.D. Raju, K.S. R. Rao, G.S. Salvapathi, P.S. S.Prasad, P. K. Rao, Aromatization of isophorone to 3,5-xylenol over Cr_2O_3/SiO_2 catalysts, *Appl. Catal. Gen.* 193 (1–2) (2000) 123–128.
[3] Quadintel, Global 3,4-Xylenol (3,4-Dimethylphenol, CAS 95-65-8) Market, 2020-2026, Quadintel, 2022. https://www.quadintel.com/toc/global-34-xylenol-34-dimethylphenol-cas-95-65-8-market/QI043.
[4] APO Research, Global 3,5-Dimethylphenol (meta-xylenol) Market Analysis and Forecast 2025-2031, APO Research, 2025. https://www.aporesearch.com/reports/chemical-material/global-35-dimethylphenol-meta-xylenol-market-analysis-and-forecast-2025-2031.
[5] C.P. Yan, X.T. Duan, W. Yan, G.H. Shang, Refinement of 2,3,5-trimethylphenol by fractional crystallization, *Technol. Dev. Chem. Ind.* 39 (2) (2010) 12–14.
[6] M.D. Qu, Z.M. E, Xylenol withdrawing in coal tar, *Chem. Technol. Econ. (10) (2005) 34–35+39.*
[7] Y. Shi, G.Y. Yu, X.Q. Wang, Experimental determination and thermodynamic modeling of solid–liquid equilibrium of 2,6-dimethylphenol, 3,5-dimethylphenol and 2,5-dimethylphenol binary and ternary systems, *Thermochim. Acta* 710 (2022) 179174.
[8] R.J.L. Andon, D.P. Biddiscombe, J.D. Cox, R. Handley, D. Harrop, E.F.G. Herington, J.F. Martin, Thermodynamic properties of organic oxygen compounds. Part I. Preparation and physical properties of pure phenol, cresols, and xylenols, *J. Chem. Soc. (1960) 5246, 1009.*
[9] X.H. Wu, Preparation method and application progress of 3,5-xylenol, *Zhejiang Chem. Ind.* 54 (10) (2023) 27–32.
[10] Y.B. Qi, J. Li, Process parameters influence on zone refining and thermodynamics analysis of 1,2-diphenylethane, *Chin. J. Chem. Eng.* 42 (2022) 338–343.
[11] B.Y. Zhang, L. Yang, H.L. Wang, C.L. Shen, Y.Y. Li, J.C. Cheng, C. Yang, Experiment and modeling of static layer melt crystallization in a crystallizer with an inner cooling tube, *J. Cryst. Growth* 593 (2022) 126739.
[12] M. Nakahara, K. Nomura, T. Washiya, T. Chikazawa, I. Hirasawa, Removal of liquid and solid impurities from uranyl nitrate hexahydrate crystalline particles in crystal purification process, *J. Nucl. Sci. Technol.* 48 (3) (2011) 322–329.
[13] M. Nakahara, K. Nomura, T. Koizumi, Purification rate of uranyl nitrate hexahydrate crystal for transuranium elements on isothermal sweating phenomenon, *Ind. Eng. Chem. Res.* 49 (22) (2010) 11661–11666.
[14] A. König, M. Stepanski, A. Kuszlik, P. Keil, C. Weller, Ultra-purification of ionic liquids by melt crystallization, *Chem. Eng. Res. Des.* 86 (7) (2008) 775–780.
[15] C.S. Luo, W.W. Chen, W.F. Han, Experimental study on factors affecting the quality of ice crystal during the freezing concentration for the brackish water, *Desalination* 260 (1–3) (2010) 231–238.
[16] J. Jung, H. Lee, K.J. Kim, Purification of acetic acid wastewater using layer melt crystallization, *Separ. Sci. Technol.* 43 (5) (2008) 1021–1033.
[17] Z.S. Fu, S.Z. Jia, Z.G. Gao, J.K. Wang, J.B. Gong, Model-based optimization of layer melt crystallization for isomers green separation, *Sep. Purif. Technol.* 378 (2025) 134657.
[18] W. Chen, S.Q. Li, S.F. Li, Purification of 2-pyrrolidone by falling film melt crystallization, *Ind. Eng. Chem. Res.* 60 (36) (2021) 13286–13292.
[19] C.X. Huang, Y. Fang, J. Wang, Y.J. Gao, C.H. Ju, Y.X. Leng, Measurement and modelling of ternary solid–liquid phase equilibrium of (DL-malic acid + maleic acid + water) from 283.15 K to 333.15 K, *J. Chem. Thermodyn.* 159 (2021) 106470.
[20] S.M. Mirpoorian, M. Vakili, S.H. Noie Baghban, P. Roohi, Determination and measurement of solid–liquid equilibrium for binary fatty acid mixtures based on NRTL and UNIQUAC activity models, *J. Therm. Anal. Calorim.* 137 (2) (2019) 679–688.
[21] H. Feng, J. Qian, Y.F. Wu, X. Xu, Y.F. Feng, J.Y. Li, N. Wang, X. Huang, T. Wang, C. Xie, H.X. Hao, Thermodynamics and kinetics of the melt crystallization of fluoroethylene carbonate, *Ind. Eng. Chem. Res.* 64 (21) (2025) 10578–10587.
[22] Q. Zhao, Y.H. Pan, Y.K. Xiong, P. Xu, Q.Y. Sun, H.M. Yin, F.M. Xue, Solubility, thermodynamic parameters, and dissolution properties of 17-α hydroxyprogesterone in 13 pure solvents, *ACS Omega* 9 (14) (2024) 16106–16117.
[23] A. Li, N. Wang, X.T. Ji, Y.H. Huang, J.W. Zhao, J. Feng, B.H. Hou, T. Wang, X. Huang, H.X. Hao, Solid–liquid equilibrium of GLA–NaCl system and its application for separating GLA and NaCl, *Ind. Eng. Chem. Res.* 63 (10) (2024) 4585–4594.
[24] A.K. Lavrinenko, I.Y. Chernyshov, E.A. Pidko, Machine learning approach for the prediction of eutectic temperatures for metal-free deep eutectic solvents, *ACS Sustain. Chem. Eng.* 11 (42) (2023) 15492–15502.
[25] D.W. Wei, S.N. Han, X. Shen, Solid–liquid phase equilibria of (*n*-octadecane with myristic, and palmitic acid) binary mixtures used as phase change materials (PCMs), *J. Chem. Thermodyn.* 101 (2016) 7–11.
[26] G. Poeti, E. Fanelli, M. Braghetti, A differential scanning calorimetric study of some phenol derivatives, *J. Therm. Anal.* 24 (2) (1982) 273–279.
[27] S.V.R. Mastrangelo, Adiabatic calorimeter for determination of cryoscopic data, *Anal. Chem.* 29 (5) (1957) 841–845.

[28] A. Codoner, I. Monzo, F. Tomas, R. Valero, Apparent dipole moments and molar volumes of dimethylphenols in some nonpolar solvents, *J. Phys. Chem.* 90 (10) (1986) 2244–2247.
[29] F.L. Ma, S.J. Xu, F. Wang, Y.Q. Bu, Y.F. Wang, L. Zhu, Measurement and correlation of 2,3-2,5-2,6-dimethylphenol solid-liquid phase equilibrium at atmospheric pressure, *Chem. Eng.* 49 (5) (2021) 48–52+68.
[30] D. Trache, K. Khimeche, R. Benelmir, A. Dahmani, DSC measurement and prediction of phase diagrams for binary mixtures of energetic materials' stabilizers, *Thermochim. Acta* 565 (2013) 8–16.
[31] U. Domańska, J. Łachwa, Thermodynamics of binary mixtures of *N*-methyl-2-pyrrolidinone and ketone. Experimental results and modelling of the (solid + liquid) equilibrium and the (vapour + liquid) equilibrium. The modified UNIFAC (Do) model characterization, *J. Chem. Thermodyn.* 37 (7) (2005) 692–704.
[32] S. Chelouche, D. Trache, S.P. Pinho, K. Khimeche, Experimental and modeling studies of binary organic eutectic systems to be used as stabilizers for nitrate esters-based energetic materials, *Fluid Phase Equilib.* 498 (2019) 104–115.
[33] R.S.B. Reddi, V.S.A.K. Satuluri, U.S. Rai, R.N. Rai, Thermal, physicochemical and microstructural studies of binary organic eutectic systems, *J. Therm. Anal. Calorim.* 107 (1) (2012) 377–385.
[34] A. Su, S.F. Li, Measurement and correlation of solid–liquid phase equilibria for binary and ternary systems consisting of *N*-vinylpyrrolidone, 2-pyrrolidone and water, *Chin. J. Chem. Eng.* 26 (4) (2018) 806–811.
[35] T.T. Shen, H. Peng, X. Ling, Experimental measurements and thermodynamic modeling of melting temperature of the binary systems *n*-$C_{11}H_{24}$–*n*-$C_{14}H_{30}$, *n*-$C_{12}H_{26}$–*n*-$C_{13}H_{28}$, *n*-$C_{12}H_{26}$–*n*-$C_{14}H_{30}$, and *n*-$C_{13}H_{28}$–*n*-$C_{15}H_{32}$ for cryogenic thermal energy storage, *Ind. Eng. Chem. Res.* 58 (32) (2019) 15026–15035.
[36] D. Trache, K. Khimeche, Study on the influence of ageing on thermal decomposition of double-base propellants and prediction of their in-use time, *Fire Mater.* 37 (4) (2013) 328–336.
[37] J.A. Nelder, R. Mead, A simplex method for function minimization, *Comput. J.* 7 (4) (1965) 308–313.
[38] Y.C. Shen, S.H. Zong, L.P. Dang, H.Y. Wei, Solubility and thermodynamics of probenecid-4, 4'-azopyridine cocrystal in pure and binary solvents, *J. Mol. Liq.* 290 (2019) 111195.
[39] W.E. Acree, Thermodynamic properties of organic compounds: enthalpy of fusion and melting point temperature compilation, *Thermochim. Acta* 189 (1) (1991) 37–56.
[40] N. Singh, N.B. Singh, U.S. Rai, O.P. Singh, Structure of eutectic melts; binary organic systems, *Thermochim. Acta* 95 (1) (1985) 291–293.